Spin-exchange-relaxation-free magnetometry with Cs vapor

M. P. Ledbetter,* I. M. Savukov, V. M. Acosta, and D. Budker†
Department of Physics, University of California at Berkeley, Berkeley, California 94720-7300, USA

M. V. Romalis
Department of Physics, Princeton University, Princeton, New Jersey 08544, USA
(Received 7 August 2007; published 13 March 2008)

We describe a Cs atomic magnetometer operating in the spin-exchange-relaxation-free (SERF) regime. With a vapor cell temperature of 103 °C we achieve intrinsic magnetic resonance widths $\Delta B=17$ μG corresponding to an electron spin-relaxation rate of 300 s^{-1} when the spin-exchange rate is $\Gamma_{SE}=14\,000$ s^{-1}. We also observe an interesting narrowing effect due to diffusion. Signal-to-noise measurements yield a sensitivity of about 400 pG/$\sqrt{\text{Hz}}$. Based on photon shot noise, we project a sensitivity of 40 pG/$\sqrt{\text{Hz}}$. A theoretical optimization of the magnetometer indicates sensitivities on the order of 2 pG/$\sqrt{\text{Hz}}$ should be achievable in a 1 cm^3 volume. Because Cs has a higher saturated vapor pressure than other alkali metals, SERF magnetometers using Cs atoms are particularly attractive in applications requiring lower temperatures.

DOI: 10.1103/PhysRevA.77.033408 PACS number(s): 32.80.Xx, 07.55.Ge, 42.65.−k

I. INTRODUCTION

Sensitive atomic magnetometers have recently found application in the field of magnetic resonance imaging [1], magnetoencephalography [2], and searches for physics beyond the standard model [3]. A recent review may be found in Ref. [4]. The most sensitive atomic magnetometers presently are the spin-exchange-relaxation-free (SERF) magnetometers [5] in which relaxation due to spin-exchange collisions is eliminated by operating in the regime where the spin-exchange rate is much greater than the rate of Larmor precession [6,7]. In Ref. [5], sensitivity of 5 pG/$\sqrt{\text{Hz}}$ was achieved with the cell operating at 190 °C using potassium atoms. Estimates of the fundamental sensitivity limit of such magnetometers are several orders of magnitude better for a 1 cm^3 volume and scale as the square root of the spin-destruction cross section.

Here we demonstrate the operation of a Cs magnetometer in the SERF regime, achieving a sensitivity of about 400 pG/$\sqrt{\text{Hz}}$ with a vapor cell temperature of only 103 °C The overlapping volume of the pump and probe beams is about 0.02 cm^3, but the effective volume, determined by diffusion, is about 1 cm^3. Based on optical rotation measurements, the projected photon shot noise limit for our experimental conditions is about 40 pG/$\sqrt{\text{Hz}}$. The spin-destruction cross section for Cs-Cs collisions is $\sigma_{SD}=2\times10^{-16}$ cm^2, about 200 times larger than for K [8]. Hence, the fundamental sensitivity of a Cs SERF magnetometer should be roughly a factor of 14 worse than that of a K SERF magnetometer. However, it is often the case that environmental noise due to, for example, Johnson currents in magnetic shields is far larger than atomic shot noise, and hence little is lost by using Cs. One of the primary motivations for investigating Cs in the SERF regime is that Cs has the highest saturated vapor pressure of all the stable alkali metals, yielding significantly lower operating temperatures. This opens up the possibility of operating in the SERF regime with low-buffer-gas-pressure paraffin-coated cells, of interest because this allows operation with significantly reduced light power. The lower temperature required for a Cs magnetometer is also attractive for applications such as NMR measurements with liquids in microfluidic channels, which is expected to be an important measurement modality in future "lab-on-a-chip" devices [9]. Cs is also of interest for a search for a permanent electric dipole moment because it is a heavy atom where CP violating effects are enhanced [10].

II. BLOCH EQUATIONS

A full treatment of the system requires the use of density matrix theory (see, for example, Ref. [11]). However, the description can be greatly simplified when the spin-exchange rate

$$\Gamma_{SE}=T_{SE}^{-1}=n\sigma_{SE}\bar{v} \tag{1}$$

(here n is the alkali-metal number density, $\sigma_{SE}\approx2\times10^{-14}$ cm^{-2} is the spin-exchange cross section, and $\bar{v}$ is the average relative velocity of the colliding alkali-metal atoms) is much faster than precession in the magnetic field, $\Gamma_{SE}\gg g_s\mu_B B/(2I+1)$. Here $g_s\approx2$ is the electron Landé factor, μ_B is the Bohr magneton, B is the magnitude of an applied magnetic field, and I is the nuclear spin. In this case the density matrix assumes a spin-temperature distribution and the ground state can be well described by Bloch equations for the electron spin polarization $\mathbf{P}=\langle\mathbf{S}\rangle/S$ [12–14] as follows:

$$\frac{d\mathbf{P}}{dt}=D\nabla^2\mathbf{P}+\frac{1}{q(P)}\left(g_s\mu_B\mathbf{P}\times\mathbf{B}+R(\mathbf{s}-\mathbf{P})-\frac{\mathbf{P}}{T_1,T_2}-\Gamma_{pr}\mathbf{P}\right). \tag{2}$$

Here D is the diffusion coefficient, $\mathbf{s}$ is the optical pumping vector along the direction of propagation of the pump with magnitude equal to the degree of circular polarization, R is

*ledbetter@berkeley.edu
†budker@berkeley.edu

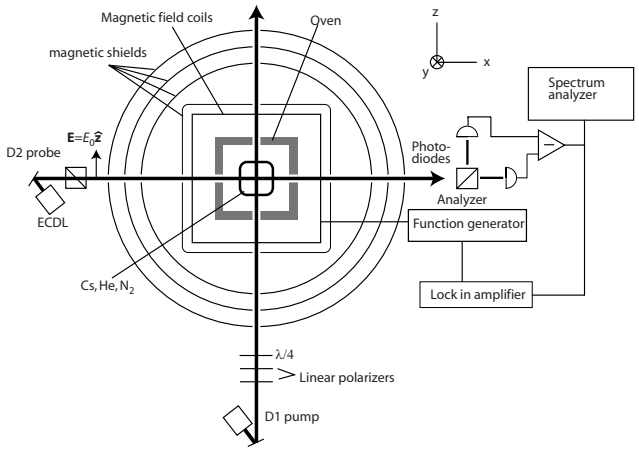

FIG. 1. (Color online) Experimental setup. A four-layer magnetic shield is employed. Circularly polarized light tuned to the $D1$ line, propagating in the z direction produces ground state orientation in the z direction. The x component of orientation S_x is detected via optical rotation of linearly polarized light, tuned to the wing of the pressure broadened $D2$ line, propagating in the x direction.

the optical pumping rate due to the pump beam, and $\Gamma_{\rm pr}$ is the rate of depolarization due to the linearly polarized probe beam. In Eq. (2), T_1 and T_2 are the relaxation times appropriate for components of the polarization parallel and transverse to $\mathbf{B}$, respectively. The quantity $q(P)$ is the nuclear slowing-down factor, which for nuclear spin $I=7/2$, is [15]

$$q(P) = \frac{2(P^6 + 17P^4 + 35P^2 + 11)}{P^6 + 7P^4 + 7P^2 + 1}. \tag{3}$$

In the low polarization limit $q(0)=22$, while in the high polarization limit $q(1)=8$. The latter limit, when all atoms are pumped into the stretched state, corresponds to the slowing-down factor for nuclear spin $I=7/2$ in the absence of spin-exchange collisions $q=2I+1=8$. The transverse relaxation time can be written

$$\frac{1}{T_2} = \Gamma_{\rm SD} + \frac{1}{T_2^{\rm SE}}, \tag{4}$$

where $\Gamma_{\rm SD}$ is the electron spin-destruction rate and $(T_2^{\rm SE})^{-1}$ is the contribution to relaxation from spin-exchange collisions. For low polarizations and small magnetic fields, relaxation due to spin exchange is quadratic in the magnetic field [7]

$$\frac{1}{T_2^{\rm SE}} = \frac{\Omega_0^2}{\Gamma_{\rm SE}} \frac{q(0)^2 - (2I+1)^2}{2}, \tag{5}$$

where $\Omega_0 = Bg_s\mu_B/q(0)$.

In some of the measurements described below, small, quasistatic magnetic fields are applied, and the conditions are such that relaxation due to spin-exchange collisions can be ignored. In our present experimental setup (see Fig. 1) optical pumping is along the z axis (the longitudinal direction) and optical rotation of the probe is due to P_x. The steady state solutions to Eq. (2) can be found by setting the left-hand side to zero, and, if diffusion is neglected, we find

$$P_x = P_0 \frac{B_x B_z - B_y \Delta B}{B^2 + \Delta B^2}, \tag{6}$$

$$P_z = P_0 \frac{B_z^2 + \Delta B^2}{B^2 + \Delta_B^2}, \tag{7}$$

where

$$\Delta B = (R + \Gamma_{\rm pr} + \Gamma_{\rm SD})/g_s\mu_B, \tag{8}$$

$$P_0 = sR/(R + \Gamma_{\rm pr} + \Gamma_{\rm SD}). \tag{9}$$

Note that Eqs. (6)–(9) are independent of the nuclear spin.

To study the effects of spin exchange, we find it convenient to apply a small rotating field $\hat{\mathbf{x}}B_1 \sin \omega t + \hat{\mathbf{y}}B_1 \cos \omega t$ in the presence of a larger bias field B_z. In this case we find the in-phase and quadrature components of P_x,

$$P_x^{(\rm in)} = -P_0 \frac{g_s\mu_B B_1}{q(P)} \frac{\Delta\omega}{(\omega - \Omega_0)^2 + \Delta\omega^2}, \tag{10}$$

$$P_x^{(\rm out)} = -P_0 \frac{g_s\mu_B B_1}{q(P)} \frac{\omega - \Omega_0}{(\omega - \Omega_0)^2 + \Delta\omega^2}, \tag{11}$$

where $\Delta\omega = (R + \Gamma_{\rm pr} + \Gamma_{\rm SD} + 1/T_2^{\rm SE})/q(P)$.

In the presence of rapid quenching of the excited state by N_2, the effects of optical pumping and the optical properties of the medium can be treated with an effective ground state formalism [16]. When the pressure broadened optical width is much larger than the hyperfine splitting, the optical pumping rate for light of frequency ν is given by [17]

$$R = \Phi\sigma = \Phi r_e c f \frac{\Delta\nu/2}{(\Delta\nu/2)^2 + (\nu - \nu_0)^2}, \tag{12}$$

where σ is the absorption cross section, $r_e = 2.8 \times 10^{-13}$ cm is the classical radius of the electron, c is the speed of light, f is the oscillator strength (roughly $1/3$ for $D1$ light and $2/3$ for $D2$ light), Φ is the photon flux per unit area and $\Delta\nu$ is the full width at half maximum of the optical transition of frequency ν_0. Equation (12) assumes light with bandwidth much less than the pressure broadened optical transition, valid for our experimental conditions. Optical rotation of linearly polarized $D2$ light, propagating in the x direction is dispersive in the detuning of the probe beam from optical resonance [16,18],

$$\phi = \frac{1}{4} l r_e c f n P_x D(\nu), \tag{13}$$

where l is the optical path length and $D(\nu) = (\nu - \nu_0)/[(\nu - \nu_0)^2 + (\Delta\nu/2)^2]$.

III. EXPERIMENTAL SETUP AND PROCEDURE

The experimental setup is shown in Fig. 1. A glass cell containing a droplet of Cs metal, 600 Torr He buffer gas (to reduce the rate at which atoms in the central part of the cell diffuse to the cell walls) and 20 Torr of N_2 (to eliminate radiation trapping and improve optical pumping efficiency)

is placed inside a four-layer set of magnetic shields. The cell has a roughly cubic profile, about 2 cm on a side. From the known rates of pressure broadening of Cs lines by helium [19], we extrapolate the FWHM of the $D1$ and $D2$ optical resonances to be $\Delta\nu=15.7$ and 14.1 GHz, respectively. The cell was heated to 103 °C (where the saturated Cs vapor concentration is about $[\mathrm{Cs}]=1.7\times10^{13}$ cm^{-3}) by flowing hot air through the space between the walls of a double-wall oven. The oven was designed so that the optical path was unperturbed by the flowing air.

The inner magnetic shield has a cubic shape with edges of length 46 cm. Magnetic fields were generated by a system of 3 coils, wound around a cubic box with symmetry axes orthogonal to each other. Including image currents results in "infinite" solenoids with square cross sections in three orthogonal directions. After degaussing, the residual fields inside the magnetic shields are on the order of 2–3 μG.

Optical pumping was accomplished by circularly polarized laser light propagating in the z direction tuned to the center of the Cs $D1$ line (the exact tuning was chosen to minimize light shifts). The pump beam was about 4 mm in diameter and originated from a Sacher Lion external cavity diode laser (ECDL) system. The linearly polarized probe beam, propagating in the x direction, had a cross section $\approx2\times3$ mm^2, and was tuned about 5 optical linewidths from the center of the pressure broadened $D2$ line (where the signal was maximized). Probe light was generated by a Newport 2010 laser system. Note that based on Eq. (13), one expects the maximum optical rotation to occur for detuning from resonance by $\Delta\nu/2$. However, the signal is the product of the transmission and optical rotation, and since our cell is optically thick (on resonance, 2 cm corresponds to 24 exponential attenuation lengths or an optical depth $(\mathrm{OD})_0=24$ under the conditions of our measurements), it was necessary to detune the laser far from resonance. The linewidth of both pump and probe lasers was on the order of 1 MHz.

Circular birefringence of the medium proportional to P_x rotates the polarization of the probe beam, which is analyzed after the cell with a balanced polarimeter. To investigate the zero-field resonance described by Eq. (6), optical rotation of the probe beam was measured as a function of a static field B_y for all other fields zeroed. B_x (B_z) can be zeroed by making use of Eq. (6): a small, slowly oscillating field (B_x) B_z is applied while B_x (B_z) is adjusted until the resulting signal is zero. To study the effects of spin-exchange broadening at nonzero fields, optical rotation was detected synchronously using a lock-in amplifier while a small rotating magnetic field $\hat{\mathbf{y}}B_1\cos\omega t+\hat{\mathbf{x}}B_1\sin\omega t$ was applied in the presence of a larger bias field B_z.

IV. EXPERIMENTAL RESULTS AND DISCUSSION

A. Zero-field resonance

In Fig. 2 the solid curves show the magneto-optical rotation of a weak probe beam ($I_{\mathrm{pr}}\approx0.5$ mW/cm^2) as a function of magnetic field B_y for two different pump intensities. The data for weak pump light $I_{\mathrm{pump}}=0.8$ mW/cm^2 is well described by Eq. (6) with $\Delta B=23$ μG. For more intense pump

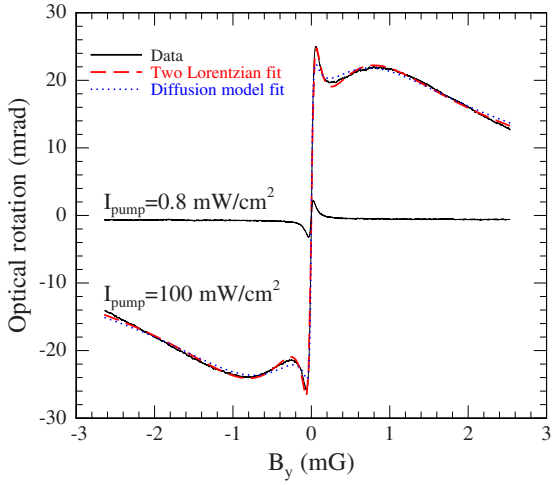

FIG. 2. (Color online) Optical rotation (solid lines) of a weak (≈0.5 mW/cm^2) probe beam as a function of B_y for pump intensities as indicated next to each trace. The dashed line overlaying the high pump intensity data is a fit to two dispersive Lorentzians, and the dotted line is a fit to a model that includes the effects of diffusion, as described in the text.

light $I_{\mathrm{pump}}=100$ mW/cm^2, optical rotation is well described by the sum of two dispersive Lorentzians with widths $\Delta B=56$ μG and $\Delta B=940$ μG, as indicated by the dashed red line. In Fig. 3 we plot the width (a) and peak-to-peak amplitude (b) of the optical rotation for the single feature observed for pump intensities below about 15 mW/cm^2 (stars) and for the nested features observed at higher pump intensities (squares and triangles). In either regime, the width is linear in light intensity. When the two features become resolved, the amplitude of the broad resonance appears saturated, while the amplitude of the narrow resonance continues to grow, approaching saturation at the highest light power.

The appearance of two resonances at high light power is essentially due to diffusion of atoms into and out of the

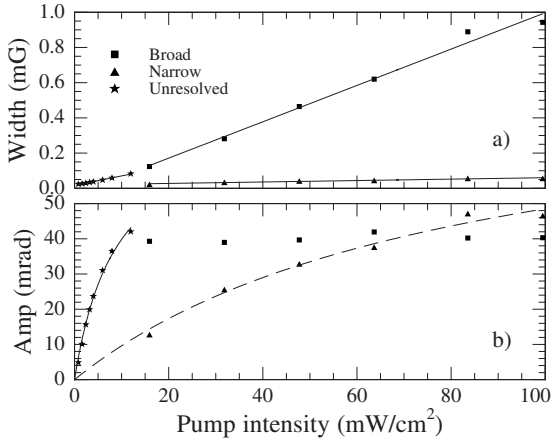

FIG. 3. (a) Half width at half maximum and (b) peak-to-peak amplitude of the broad, narrow, and unresolved features observed in the zero-field resonance shown in Fig. 2, as a function of pump power. The lines overlaying the data in (a) are fits described in the text. The solid and dashed lines in (b) serve to guide the eye.

pump beam. Similar narrowing effects due to diffusion have been observed in the context of electromagnetically induced transparency in buffer gas cells [21]. Nested resonances have also been observed in the context of nonlinear magneto-optical rotation in paraffin coated cells [22,23]. The presence of diffusion results in a layer of polarized atoms with thickness $\approx\sqrt{qD/\Gamma_{SD}}$, with polarization and rate of power broadening differing from those inside the pump beam. When R is small compared to Γ_{SD}, the extra broadening inside the pump beam is negligible and the contributions to magneto-optical rotation from atoms inside and outside the pump beam are similar, yielding a single feature. As R becomes large compared to Γ_{SD}, the region inside the pump beam contributes to the broad part of the magneto-optical rotation curve, while the region outside the beam suffers much less broadening, resulting in the narrow part of the magneto-optical rotation curve. A rigorous description of the nested resonance can be obtained by including the contribution from diffusion to Eq. (2). In general, the solutions are quite complicated, however, by neglecting the polarization dependence of the slowing-down factor, analytical solutions can be found for the case of one-dimensional diffusion in Cartesian coordinates, valid in the limit that the probe beam is considerably smaller than the pump beam. Figure 2 shows a fit to the analytical solution, with the beam diameter $d=2.6$ mm, $qD=15$ cm^2/s, $R=18\,000$ s^{-1}, $\Gamma_{SD}=465$ s^{-1} as free parameters. From previous measurements of the diffusion constant [20], we estimate $D=0.46$ cm^2/s for the buffer gas content of our cell, so qD falls somewhere between 3.4 cm^2/s and 10.1 cm^2/s for q in the range of 8 and 22. The pump rate R and the spin-destruction rate Γ_{SD} are within a factor of 2 of the values obtained from the low light-power behavior (see below). Given that the model neglects the polarization dependence of the slowing-down factor, we consider this relatively good agreement. We suspect that a full solution taking into account the polarization dependence of the slowing-down factor will yield greater accuracy of these basic parameters.

From the low light-power data, we can obtain an independent measurement of the intrinsic relaxation rate Γ_{SD}. Overlaying the low light-power data in Fig. 3(a) is a linear fit based on Eq. (8) with $R=\eta I_{pump}$ yielding $\eta=93$ s^{-1}/(mW/cm^2) and zero light-power width $\Delta B_0=17\pm3$ μG corresponding to $\Gamma_{SD}=300\pm52$ s^{-1}. This can be compared to the expected spin-destruction rate based on previous measurements of the spin-destruction cross sections

$$\Gamma_{SD}=[\mathrm{Cs}]\bar{v}^{\mathrm{Cs}}\sigma_{SD}^{\mathrm{Cs}}+[\mathrm{He}]\bar{v}^{\mathrm{He}}\sigma_{SD}^{\mathrm{He}}+[\mathrm{N_2}]\bar{v}^{\mathrm{N_2}}\sigma_{SD}^{\mathrm{N_2}}. \quad (14)$$

Here, $\sigma_{SD}^{Cs}=2\times10^{-16}$ cm^2 [8], $\sigma_{SD}^{He}=3\times10^{-23}$ cm^2 [20], and $\sigma_{SD}^{N_2}=6\times10^{-22}$ cm^2 [20] are the spin-destruction cross sections for Cs-Cs, Cs-He, and Cs-N_2 collisions, respectively. The mean relative velocity $\bar{v}^X$ differs between colliding pairs, and hence the superscript in Eq. (14). The contributions to the spin-destruction rate from Cs, He, and N_2 collisions are 119 s^{-1}, 88 s^{-1}, and 32 s^{-1}, respectively, yielding a total spin-destruction rate $\Gamma_{SD}=240$ s^{-1}, in reasonable agreement with the present measurements.

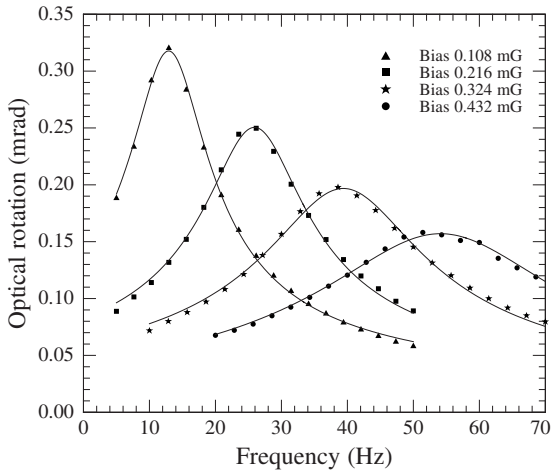

FIG. 4. Response of magnetometer to a small rotating magnetic field of magnitude $B_1=0.55$ μG transverse to a larger bias field B_z for several different values of B_z. For these data the pump and probe intensities were 4 mW/cm^2 and 1.3 mW/cm^2, respectively.

B. Spin-exchange effects

To explore the effects of spin exchange on transverse relaxation we apply a bias magnetic field in the z direction (along the pump beam) and a small transverse rotating magnetic field to excite a component of polarization transverse to the bias field. In-phase and quadrature components of the resulting optical rotation signal are detected synchronously using a lock-in amplifier. In Fig. 4 we show the quadrature sum of the in- and out-of-phase optical rotation signals as a function of frequency for several different values of the bias magnetic field. Overlaying the data are fits to $a\Delta\omega/\sqrt{(\omega-\Omega_0)^2+\Delta\omega^2}$ [see Eqs. (10) and (11)]. For these data, the pump and probe intensity were about 4 and 1.3 mW/cm^2, respectively. Based on the data shown in Fig. 3, these intensities produce power broadening by about a factor of 2 over the zero light-power width, however, the slowing-down factor, determined from a linear fit to Ω_0, was very nearly $q=22$ indicating that the polarization was quite low [see Eq. (3)].

In Fig. 5 we plot the half width at half maximum $\Delta\omega$ of the resonances shown in Fig. 4 as a function of the bias field. Overlaying the data is a fit based on Eq. (5) with $\Delta\omega=[q(0)T_2]^{-1}$ and $\Omega_0=g_s\mu_B B/q(0)$, allowing for a constant offset due to spin-destruction collisions, diffusion and power broadening, yielding a spin-exchange rate $\Gamma_{SE}=14\,300\pm350$ s^{-1}. For $n=1.7\times10^{13}$ cm^{-3} obtained from the saturated vapor pressure curve, Eq. (1) gives a spin-exchange rate of about 12 000 s^{-1}. Temperature fluctuations of two or three degrees could cause significant variations in the vapor pressure, and hence we consider this reasonable agreement with measurements of spin-exchange broadening.

C. Sensitivity

We evaluate the performance of the magnetometer by monitoring the noise level at the output of the balanced polarimeter using a Stanford Research Systems SR770 spec-

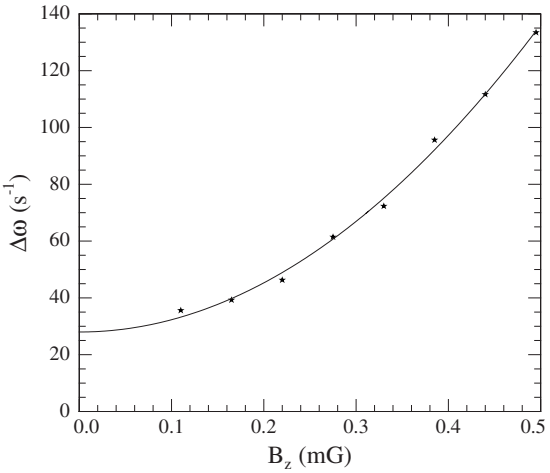

FIG. 5. Half width at half maximum of the bias-field resonances shown in Fig. 4 as a function of magnetic field.

trum analyzer. To calibrate the magnetometer, we apply a small oscillating field $B_y = B_1 \cos \omega t$ with $B_1 = 0.55$ μG at several different frequencies. The resulting spectra are shown as solid lines in Fig. 6. Each trace in Fig. 6 is the result of averaging ten spectra obtained during 1 s intervals, yielding a spectral resolution of 1 Hz. The triangular shape of the calibration peaks is due to the use of the built-in Hann windowing function with finite spectral resolution. For these data, the pump and probe intensities were 100 $\mathrm{mW/cm^2}$ and 4 $\mathrm{mW/cm^2}$, respectively, and all three components of the dc magnetic field have been zeroed. The sensitivity, in $\mathrm{G_{rms}/\sqrt{Hz}}$ is determined by $\delta B = B_1/(\sqrt{2}S/N)$ yielding a sensitivity of about 400 $\mathrm{pG_{rms}/\sqrt{Hz}}$ at 30 Hz and about 600 $\mathrm{pG_{rms}/\sqrt{Hz}}$ at 10 Hz. The dashed line in Fig. 6 represents the estimated photon shot noise limit in the difference of the photocurrents for unit bandwidth $\delta I = \sqrt{4eI}$, where I is the photocurrent in one channel of the balanced polarimeter, yielding a photon shot noise limited sensitivity of about 40 $\mathrm{pG/\sqrt{Hz}}$ at 10 Hz. Several possible sources of the extra noise are (1) real fluctuations of the ambient field (either due to imperfect magnetic shielding or noise in the current source), (2) fluctuations in the pump power coupled with misalignment of the pump and probe beams, or (3) vibrations of the probe relative to the pump in the plane common to both beams. Optimization of geometry to maximize the overlapping volumes of the pump and probe beams will likely yield improvements in the photon shot noise limit.

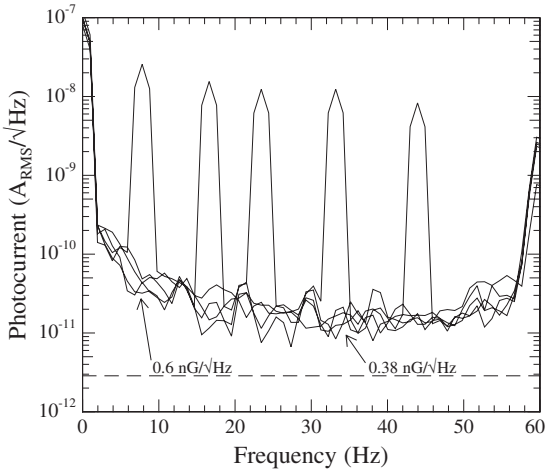

FIG. 6. Fourier transform of magnetometer signal (solid lines) with calibration peaks of amplitude $B_1 = 0.55$ μG applied at several different frequencies. The dashed line represents photon shot noise.

V. CONCLUSIONS

We demonstrated a Cs atomic magnetometer in the spin-exchange-relaxation-free regime. The primary advantage of using Cs is the ability to work at lower temperatures. Future work with atomic magnetometers in the context of microfluidic NMR will make use of this feature. At 103 °C we realized magneto-optical rotation features with intrinsic linewidths of 17 μG corresponding to a relaxation rate of about 300 $\mathrm{s^{-1}}$ when the spin-exchange rate was about $\Gamma_{\mathrm{SE}} = 14\,000$ $\mathrm{s^{-1}}$. We achieved a sensitivity of 400 $\mathrm{pG/\sqrt{Hz}}$. Based on estimates of the photon shot noise, we project a sensitivity of about 40 $\mathrm{pG/\sqrt{Hz}}$. We suspect that the demonstrated sensitivity was limited by pump laser noise and ambient magnetic field noise. Theoretical optimization of the magnetometer (presented in the Appendix below) indicates it should be possible to achieve sensitivity on the order of 2 $\mathrm{pG/\sqrt{Hz}}$ in a 1 $\mathrm{cm^3}$ volume. We believe the primary reason for falling short of this level is suboptimal geometry (probe beam cross section was only 2×3 $\mathrm{mm^2}$) detuning and light power of both pump and probe.

ACKNOWLEDGMENTS

This work was supported by an ONR MURI grant.

APPENDIX: THEORETICAL OPTIMIZATION

We now present a theoretical optimization of the magnetometer, maximizing sensitivity to small, quasistatic fields. The analysis is similar to Refs. [24,25], in that spin-projection noise and photon shot noise are considered independently (noise due to light shifts is not considered, because in principle, it can be eliminated by orthogonality of pump and probe beams [25]). Spin-projection noise is typically written as

$$\delta B \approx \frac{1}{\gamma\sqrt{NtT_2}}, \tag{A1}$$

where γ is the gyromagnetic ratio, N is the number of atoms, t is the measurement time, and T_2 is the transverse relaxation time. In the SERF regime $T_2 = q(P)/\Gamma_{\mathrm{SD}}$ and $\gamma = g_s \mu_B / q(P)$ both depend on the nuclear slowing-down factor. Inserting these expressions into Eq. (A1), one might conclude that the atomic shot noise limit scales as $\sqrt{q(P)}$. However, it turns out that the nuclear slowing-down factor drops out of the problem. The reasons are somewhat subtle, so we go into some detail.

Spin-projection noise arises (in the present geometry) due to uncertainty in the x component of angular momentum F_x,

defined as $\Delta F_x = \sqrt{\langle F_x^2\rangle - \langle F_x\rangle^2}$. For a spin-temperature distribution with polarization in the z direction $\rho \propto e^{\beta F_z}$, where $\beta = \ln(1+P)/(1-P)$ is the spin-temperature parameter [11] $\langle F_x\rangle = 0$. Thus $\Delta F_x = \sqrt{\mathrm{Tr}(\rho F_x^2)}$. Evaluation of this trace results in $\Delta F_x(P) = \sqrt{q(P)/4}$ per atom with ρ normalized so that $\mathrm{Tr}\,\rho = 1$. Assuming that $N = nV$ uncorrelated atoms are involved in the measurement, the ensemble averaged uncertainty scales as $1/\sqrt{nV}$,

$$\delta F_x(P) = \sqrt{\frac{q(P)}{4nV}}. \tag{A2}$$

In the large polarization limit, $\delta F_x(1) = \sqrt{2/nV}$. This limit can be obtained from the angular momentum commutation relations $[F_x, F_y] = iF_z$, which yield the minimum uncertainty $\sqrt{|\langle F_z\rangle|}/2$. If all the atoms are in the stretched state, corresponding to $P=1$, $\langle F_z\rangle = 4$, we have, again assuming uncorrelated atoms, $\delta F_x = \sqrt{2/nV}$. The uncertainty in the low polarization limit is somewhat larger, $\delta F_x(0) = \sqrt{11/2nV}$. This limit can also be verified by noting that for an unpolarized sample $\rho = 1/(2S+1)(2I+1)$ and $\mathrm{Tr}(\rho F_x^2) = \mathrm{Tr}(\rho F_z^2)$. As an aside, we note that the reduction in uncertainty δF_x with increasing polarization only occurs for angular momentum greater than 1/2.

After measuring continuously for time t long compared to the lifetime of the polarization $q(P)/(R+\Gamma_{\mathrm{pr}}+\Gamma_{\mathrm{SD}})$, the uncertainty is [24,26]

$$\langle \delta F_x\rangle_t = \delta F_x \sqrt{\frac{2q(P)}{(R+\Gamma_{\mathrm{pr}}+\Gamma_{\mathrm{SD}})t}}, \tag{A3}$$

$$= \frac{q(P)}{\sqrt{2t(R+\Gamma_{\mathrm{pr}}+\Gamma_{\mathrm{SD}})nV}}. \tag{A4}$$

In a spin-temperature distribution, the ratio of the total angular momentum to that stored in the electron is given by $q(P)$, $\langle \mathbf{F}\rangle = [q(P)/2]\mathbf{P}$ [11] and thus

$$\delta P_x = \frac{2}{q(P)}\langle \delta F_x\rangle_t = \sqrt{\frac{2}{t(R+\Gamma_{\mathrm{pr}}+\Gamma_{\mathrm{SD}})nV}}. \tag{A5}$$

The uncertainty δB_y in a measurement of B_y is related to flucutations of P_x via Eq. (6) (for all other fields zeroed),

$$\delta B_y = \frac{R+\Gamma_{\mathrm{pr}}+\Gamma_{\mathrm{SD}}}{g_s\mu_B}\frac{\delta P_x}{P_z}. \tag{A6}$$

Inserting Eq. (A5) into Eq. (A6) we find that the spin-projection noise is

$$\delta B_{\mathrm{spn}} = \frac{1}{g_s\mu_B P_z}\sqrt{\frac{2(R+\Gamma_{\mathrm{pr}}+\Gamma_{\mathrm{SD}})}{nVt}}. \tag{A7}$$

It is interesting to note that this result is independent of any nuclear slowing-down factors. Neglecting broadening due to the probe beam, the minimum value of spin-projection noise

$$\delta B_{\mathrm{spn}}^{\mathrm{min}} = 3\sqrt{3/2}\frac{1}{g_s\mu_B}\sqrt{\frac{\Gamma_{\mathrm{SD}}}{nVt}} \tag{A8}$$

is obtained when $R = 2\Gamma_{\mathrm{SD}}$.

We now address photon shot noise. To simplify the analysis, we assume that the volume V occupied by the sample is a cube with sides of length l, fully illuminated by both pump and probe. If the probe beam is detuned far from resonance so that the medium is optically thin, optical rotation drops slowly, scaling as $D(\nu) \approx 1/(\nu-\nu_0)$, compared to absorption which scales as $1/(\nu-\nu_0)^2$, a very favorable situation. In this case, photon shot noise in the optical rotation angle is given by $\delta\phi = 1/2\sqrt{\Phi_0 l^2 t}$, where Φ_0 is the probe photon intensity and l^2 is the cross section of the probe beam. Combining this with Eqs. (13) and (A6), the photon shot noise contribution to magnetic field sensitivity is

$$\delta B_{\mathrm{psn}} = \frac{1}{g_s\mu_B P_z}\frac{2(R+\Gamma_{\mathrm{pr}}+\Gamma_{\mathrm{SD}})}{lr_e cfnD(\nu)\sqrt{\Phi_0 l^2 t}}. \tag{A9}$$

This can be rearranged

$$\delta B_{\mathrm{psn}} = \frac{1}{g_s\mu_B P_z\sqrt{nVt}}\frac{2(R+\Gamma_{\mathrm{pr}}+\Gamma_{\mathrm{SD}})}{\sqrt{\Gamma_{\mathrm{pr}}(\mathrm{OD})_0}}, \tag{A10}$$

where $(\mathrm{OD})_0 = 2r_e cfnl/\Delta\nu$ is the optical depth on resonance and

$$\Gamma_{\mathrm{pr}} = \Phi_0 r_e cf\frac{\Delta\nu/2}{(\nu-\nu_0)^2} \tag{A11}$$

is the probe rate for far detuned light.

Adding spin-projection noise Eq. (A7) and photon shot noise Eq. (A10) in quadrature, yields

$$\delta B = \frac{1}{g_s\mu_B P_z\sqrt{nVt}}\sqrt{2(R+\Gamma_{\mathrm{pr}}+\Gamma_{\mathrm{SD}}) + \frac{4(R+\Gamma_{\mathrm{pr}}+\Gamma_{\mathrm{SD}})^2}{\Gamma_{\mathrm{pr}}(\mathrm{OD})_0}}. \tag{A12}$$

For a cubic volume of 1 cm^3 and a density of $n = 1.7\times10^{13}$ cm^{-3}, the resonant optical depth $(\mathrm{OD})_0 \approx 12$ for the buffer gas contents of our cell. Assuming a spin-destruction rate $\Gamma_{\mathrm{SD}} = 300$ s^{-1} obtained in the experiment at 103 °C, Eq. (A12) reaches a minimum of about 2.4 $\mathrm{pG}/\sqrt{\mathrm{Hz}}$ with pump and probe rates $R = 710$ s^{-1} and $\Gamma_{\mathrm{pr}} = 91$ s^{-1} (here we have assumed that a bandwidth of 1 Hz corresponds to a measurement time of 0.5 s).

Further inspection of Eq. (12) shows that the second term underneath the radical can be made small if the resonant optical depth is large. In this case, Γ_{pr} can be made small so that the first term underneath the radical is minimized. In the limit of infinite resonant optical depth Eq. (A12) is optimized for $R = 2\Gamma_{\mathrm{SD}}$ and $\Gamma_{\mathrm{pr}} \approx 0$, in which case Eq. (A12) reduces to Eq. (A8). For a volume of 1 cm^3 and a density of $n = 1.7\times10^{13}$ cm^{-3}, and spin-destruction rate $\Gamma_{\mathrm{SD}} = 300$ s^{-1} obtained in the experiment at 103 °C, Eq. (A8) evaluates to about 1.2 $\mathrm{pG}/\sqrt{\mathrm{Hz}}$. Slightly better sensitivity may be achieved by operating at higher densities where Cs-Cs collisions completely dominate the collisional spin-destruction rate [see the discussion following Eq. (14)].

The above analysis indicates that optimal sensitivity is achieved when the probe is tuned sufficiently far from resonance so that the medium is optically thin, minimizing photon shot noise. However, technical sources of noise due to,

e.g., vibrations or air currents, are often much larger than photon shot noise. In this case, it is desirable to tune the laser closer to optical resonance so that the optical rotation due to small magnetic fields is larger than other sources of noise. Finally, we note that the optimal tuning of the probe light depends on the particulars of the probing scheme. For example, Ref. [27] considers the case of nonlinear magneto-optical rotation, where optimal sensitivity is achieved when the probe is tuned so that there is roughly one optical depth. The primary reason for the difference is that optical rotation in that case scales (similarly to absorption) as the inverse square of the detuning.

[1] S. Xu *et al.*, Proc. Natl. Acad. Sci. USA, arXiv:10.1073/pnas.0605396103 (2006).
[2] H. Xia, A. B. Baranga, D. Hoffman, and M. V. Romalis, Appl. Phys. Lett. **89**, 211104 (2006).
[3] D. Bear, R. E. Stoner, R. L. Walsworth, V. A. Kostelecky, and C. D. Lane, Phys. Rev. Lett. **85**, 5038 (2000); **89**, 209902(E) (2002).
[4] D. Budker and M. V. Romalis, Nat. Phys. **3**, 227 (2007).
[5] I. K. Kominis, T. W. Kornack, J. C. Allred, and M. V. Romalis, Nature (London) **422**, 596 (2003).
[6] W. Happer and H. Tang, Phys. Rev. Lett. **31**, 273 (1973).
[7] W. Happer and A. C. Tam, Phys. Rev. A **16**, 1877 (1977).
[8] N. D. Bhaskar, J. Pietras, J. Camparo, W. Happer, and J. Liran, Phys. Rev. Lett. **44**, 930 (1980).
[9] M.P. Ledbetter, D. Budker, I. M. Savukov, V. Shah, S. Knappe, J. Kitching, S. Xu, D. Michalak, and A. Pines (unpublished).
[10] S. A. Murthy, D. Krause, Z. L. Li, and L. R. Hunter, Phys. Rev. Lett. **63**, 965 (1989).
[11] S. Appelt, A. B. Baranga, C. J. Erikson, M. Romalis, A. R. Young, and W. Happer, Phys. Rev. A **58**, 1412 (1998).
[12] J. C. Allred, R. N. Lyman, T. W. Kornack, and M. V. Romalis, Phys. Rev. Lett. **89**, 130801 (2002).
[13] T. W. Kornack and M. V. Romalis, Phys. Rev. Lett. **89**, 253002 (2002).
[14] S. J. Seltzer and M. V. Romalis, Appl. Phys. Lett. **85**, 4804 (2004).
[15] I. M. Savukov and M. V. Romalis, Phys. Rev. A **71**, 023405 (2005).
[16] W. Happer and B. Mathur, Phys. Rev. **163**, 12 (1967).
[17] S. Appelt, A. B. Baranga, A. R. Young, and W. Happer, Phys. Rev. A **59**, 2078 (1999).
[18] T. W. Kornack, Ph.D. thesis, Princeton University, 2005 (unpublished).
[19] A. Andalkar and R. B. Warrington, Phys. Rev. A **65**, 032708 (2002).
[20] N. Beverini, P. Minguzzi, and F. Strumia, Phys. Rev. A **4**, 550 (1971).
[21] Y. Xiao, I. Novikova, D. F. Phillips, and R. L. Walsworth, Phys. Rev. Lett. **96**, 043601 (2006).
[22] D. Budker, V. Yashchuk, and M. Zolotorev, Phys. Rev. Lett. **81**, 5788 (1998).
[23] E. W. McDaniel and E. A. Mason, *The Mobility and Diffusion of Ions in Gases* (Wiley, New York, 1973).
[24] I. M. Savukov, S. J. Seltzer, M. V. Romalis, and K. L. Sauer, Phys. Rev. Lett. **95**, 063004 (2005).
[25] M. Auzinsh, D. Budker, D. F. Kimball, S. M. Rochester, J. E. Stalnaker, A. O. Sushkov, and V. V. Yashchuk, Phys. Rev. Lett. **93**, 173002 (2004).
[26] W. A. Gardner, *Introduction to Random Processes* (McGraw Hill, New York, 1990).
[27] S. M. Rochester and D. Budker, J. Mod. Opt. **49**, 2543 (2002).